

Combining Path Analysis with Time-resolved Functional Magnetic Resonance Imaging: The Neurocognitive Network Underlying Mental Rotation

Christine Ecker, Michael J. Brammer, and Steven C. Williams

Abstract

■ There is strong evidence to suggest that the complex cognitive process underlying mental rotation does not have a discrete neural correlate, but is represented as a distributed neural system. Although the neuroanatomical nodes of this so-called rotation network are well established, there is as yet little empirical evidence to indicate how these nodes interact during task performance. Using an optimized, event-related paradigm, this study aimed to test a previously proposed hypothetical neurocognitive network for mental rotation in female subjects with path analysis, and to examine changes in effective connections across different levels of task difficulty. Path analysis was carried out in combination with a time-resolved functional magnetic resonance imaging (fMRI) analysis in order to relate the observed changes on the network level to changes in specific temporal characteristics of

the hemodynamic response function on the level of individual neuroanatomical nodes. Overall, it was found that the investigated sequential model did not provide an adequate fit to the data and that a model with parallel information processing was superior to the serial model. This finding challenges traditional cognitive models describing the complex cognitive process underlying mental rotation by a set of sequentially organized, functionally distinct processing stages. It was further demonstrated that the observed interregional effective connectivity changes with the level of task demand. These changes were directly related to the time course of the experimental paradigm. The results of path analysis in fMRI should therefore only be interpreted in the light of a specific experimental design and should not be considered as general indicators of effective connections. ■

INTRODUCTION

Functional neuroimaging studies have provided strong evidence to suggest that the complex cognitive process underlying mental rotation does not have a discrete neural correlate, but is represented as a distributed neural system. This so-called rotation network comprises parietal regions (Harris et al., 2000; Carpenter, Just, Keller, Eddy, & Thulborn, 1999; Iwaki, Ueno, Imada, & Tonoike, 1999), several areas of the motor system (Vingerhoets, de Lange, Vandemaele, Deblaere, & Achten, 2002; Ganis, Keenan, Kosslyn, & Pascual-Leone, 2000; Kosslyn, DiGirolamo, Thompson, & Alpert, 1998; Parsons et al., 1995), as well as visual-system components (Barnes et al., 2000; Alivisatos & Petrides, 1997; Cohen et al., 1996). Although parietal regions have been found to be consistently activated across several object categories and rotation strategies, the involvement of the visual and motor system has predominantly been linked to stimulus-specific strategies employed in rotation tasks. Depictive theories suggest that subjects employ a visuospatial holistic strategy in which objects are

pictured in mind and then rotated continuously, thus recruiting the visual system (Kosslyn, 1996). Egocentric theories, on the other hand, assume that subjects imagine physically turning objects, and thus, involve motor processes (Kosslyn, Ganis, & Thompson, 2001).

Although the neuroanatomical nodes of the rotation network are well established, there is as yet little empirical evidence to indicate how these nodes interact during task performance. Several previous publications have investigated the neurocognitive network involved in processing conventional imagery tasks (Formisano et al., 2002). Notably, a study by Mechelli, Price, Friston, and Ishai (2004) has demonstrated that visual imagery activates a network of occipito-temporal, parietal, and frontal regions. The authors suggest that top-down processes originating in superior-parietal areas contribute to the generation and maintenance of mental images, whereas bottom-up processes originating in early visual areas modulate visual perception (Mechelli et al., 2004). Mental rotation is, however, an unconventional imagery task in that it not only requires the generation and maintenance of presented objects but also their active manipulation. To our knowledge, only one

Institute of Psychiatry, London

publication has as yet described a cortical network for solving mental rotation tasks. Jordan, Wustenberg, Heinze, Peters, and Jancke (2002) suggested that women and men exhibit different cortical activation patterns during mental rotation tasks, and proposed two gender-specific pathways. In the “male” pathway, mental rotation is assumed to be processed in a strictly sequential manner, involving exclusively forward projections from the occipital cortex to premotor regions (PMd) via dorsal extrastriate areas (DE) and parietal regions. The “female” pathway (see Figure 1), on the other hand, includes the inferior temporal lobe (ITp) as an additional network component. The ITp is believed to be reciprocally connected with DE, thus assuming parallel information processing within the visual subcomponents (Jordan et al., 2002). So far, the model proposed by Jordan et al. (2002) is, however, merely a hypothetical construct requiring empirical validation. The first aim of the present study was therefore to investigate the validity of the Jordan model in a female subject group using structural equation modeling (SEM), and to examine changes in effective connectivity across different levels of task difficulty.

Although there are several studies investigating connectivity while the brain is “at rest” (Tian et al., 2006;

Beckmann, DeLuca, Devlin, & Smith, 2005), most previous publications examine brain connectivity in the presence of an experimental paradigm (Grady, Furey, Pietrini, Horwitz, & Rapoport, 2001; Friston & Buchel, 2000). So far, little is, however, known about the optimization of experimental paradigms for connectivity analysis and the influence of the chosen experimental designs on the observed cortical interactions. In SEM, the strength of a cortical interaction is indicated by a path coefficient quantifying the average influence of one region of interest (ROI) onto another in a given time interval (McIntosh & Gonzalez-Lima, 1994). Despite the fact that path coefficients denote the degree of effective connectivity between neuroanatomical nodes (Friston, Frith, Liddle, & Frackowiak, 1993), ultimately, they still reflect the degree of temporal coherences between two ROIs in the presence of additional network nodes. One of the most significant factors determining the degree of temporal coherences between brain regions is the employed experimental design. Different sets of path coefficients might therefore be observed depending on how the overall time course of the experiment is subdivided.

The second aim of this study was to address several methodological issues regarding the choice of experimental design for connectivity analysis in general, and using SEM in particular. To investigate the effect of the experimental design on the observed path coefficients and to further explore the meaning of path coefficients, SEM was combined with a time-resolved functional magnetic resonance imaging (fMRI) analysis, which has been published previously (Ecker, Brammer, David, & Williams, 2006). This way, the results on the network level could be related to specific changes in temporal characteristics of the hemodynamic response on the level of individual network nodes.

Finally, we aim to examine whether a model with reciprocal or feedback connections is superior over the predominantly serial model proposed by Jordan et al. (2002). This finding could challenge traditional cognitive models describing the complex cognitive process underlying mental rotation by a set of functionally distinct processing stages.

METHODS

General Model Assumptions and Hypotheses

In the present study, an event-related paradigm was used to investigate changes in effective connectivity across different levels of task difficulty within the rotation network. This paradigm was optimized for connectivity analysis using SEM in several respects.

Firstly, individual trials were separated by a comparatively long interstimulus interval (ISI), after which the hemodynamic response function (HRF) should have decayed to baseline (Kwong et al., 1992). Trials can therefore be considered to be separate events allowing subsequent concatenation of the condition-specific time

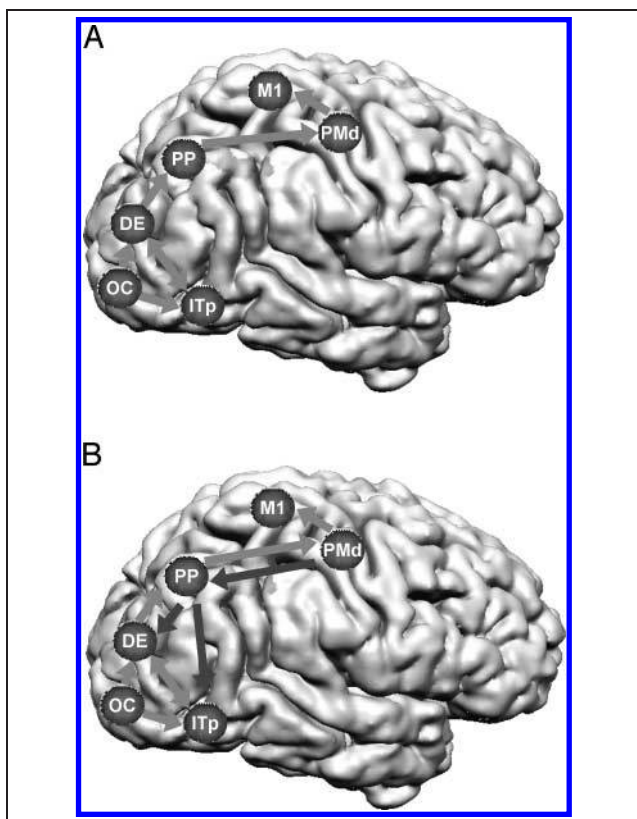


Figure 1. Schematic display of the neurocognitive network underlying mental rotation proposed by Jordan et al. (2002). (A) The original model was extended by including M1 as additional network node. (B) The newly proposed rotation network with feedback connections.

series. The concatenation of the condition-specific time series is problematic in conventional event-related fMRI paradigms, where short ISIs are used to minimize the duration of the experiment. At short ISIs, however, the hemodynamic responses (HRF) of individual events overlap, thus making it impossible to allocate signal intensity values to specific conditions.

Secondly, to investigate the relationship between the experimental paradigm and the obtained path coefficients, the overall time course of the experiment was subdivided into temporally distinct subprocesses: (1) time course of perceptual process as determined by stimulus duration, (2) time course of the cognitive process as identified by reaction times (RTs), and (3) time course associated with motor execution at the end of the cognitive process. As demonstrated by previous investigation, the temporal parameters of the HRF in specific neuroanatomical nodes of the rotation network can be altered as a function of RTs. For instance, a study by Richter et al. (2000) and Richter, Ugurbil, Georgopoulos, and Kim (1997) has shown that the full width at half maximum (FWHM) of the HRF increases significantly with RTs in the premotor area, in the supplementary motor cortex, and in the superior parietal lobe, thus suggesting that these regions are likely to participate in the mental spatial transformation itself. In addition, RTs were positively correlated with the latency of the response in the primary motor cortex, as would be expected if the functional activation observed in M1 was related to the button press (Richter et al., 1997, 2000). In regions that are linked to perceptual processes, the temporal characteristics of the HRF should be constant across conditions as long as the stimulus duration is the same in all conditions (see Figure 2A).

The size and direction of change in interregional connectivity following alterations in temporal characteristics can be predicted using models of the HRF during event-related stimulus presentation. These models were generated on the basis of conventionally used gamma functions and varied in amplitude, phase, and width. Subsequently, changes in zero-order correlation coefficients (r) between the initial function and its temporal variants can be identified for each parameter. As shown in Figure 3, differences in signal amplitude did not lead to any significant change in r . Alterations in width or phase of the models decreased r considerably, especially when the phase parameter was changed.

Figure 2 also illustrates the very definition of general connectivity, which is defined as the temporal coherence between physiological events (Friston et al., 1993). It was thus expected that region-specific alterations in the temporal parameters of the HRF would be accompanied by changes in effective connections on the network level. More specifically, significant changes in effective connections should only be seen in paths linking a region whose FWHM varies with RTs, and a region whose FWHM is constant across conditions. Path coeffi-

cients linking two regions whose FWHMs change in a similar fashion (i.e., the FWHM of the HRF in both ROIs varies with RTs, or is constant across conditions) should not change with the level of task difficulty (see Figure 2B).

Subjects

Ten right-handed female volunteers between 20 and 30 years of age participated in this study. All participants were in good general health and exhibited normal eyesight. These subjects were reported previously in Ecker et al. (2006). All subjects gave written informed consent for the procedure in accordance with protocols approved by the South London and Maudsley NHS Trust Ethics Committee.

Experimental Design

Details of the experimental design and stimuli used in this investigation can be found elsewhere (Ecker et al., 2006). In brief, subjects viewed pairs of cubic structures similar to those used by Shepard and Metzler (1971). These structures included 10 different 3-D objects of which half were mirror images (isomers) of existing figures. The object pairs were presented in four different conditions according to the angular disparity: (1) 0° (2 identical objects at the same orientation), (2) 20°, (3) 60°, and (4) 100° angular disparity. The 3-D objects in each pair were either the same (same pair) or mirror images (different pair). In the same pair presentation, the two objects could be rotated into congruence with each other. In different pair presentation, the two objects differed by a reflection, as well as a rotation in either x or z dimension and could not be rotated into congruence. Subjects were asked to decide whether the objects were the same or mirror images and to indicate their choice via button press. Event-related fMRI with constant stimulus duration (SD) and constant ISI was used in this study. In all trials (20 per condition), the 3-D objects were presented for a period of 10 sec, followed by a fixation cross (baseline) (see Figure 3A). To keep the SD constant, the objects did not disappear from the screen after subjects indicated their choice by button press. Instead, objects were presented for an additional period of Δt with $\Delta t = 10 \text{ sec} - \text{RT} \text{ (sec)}$. Subjects were instructed to avoid repeated object rotation by focusing their eye gaze on one of the presented objects. This experimental design was chosen in order to desynchronize RT and SD by a time equal to Δt . Individual trials were separated by an ISI of 6 sec, after which the HRF should have decayed to the baseline level (Kwong et al., 1992).

Data Acquisition

A 1.5-T GE Signa Neuro-optimized System (General Electric, Milwaukee, WI, USA) was used to acquire 760 blood oxygenation level-dependent (BOLD) T2*-weighted

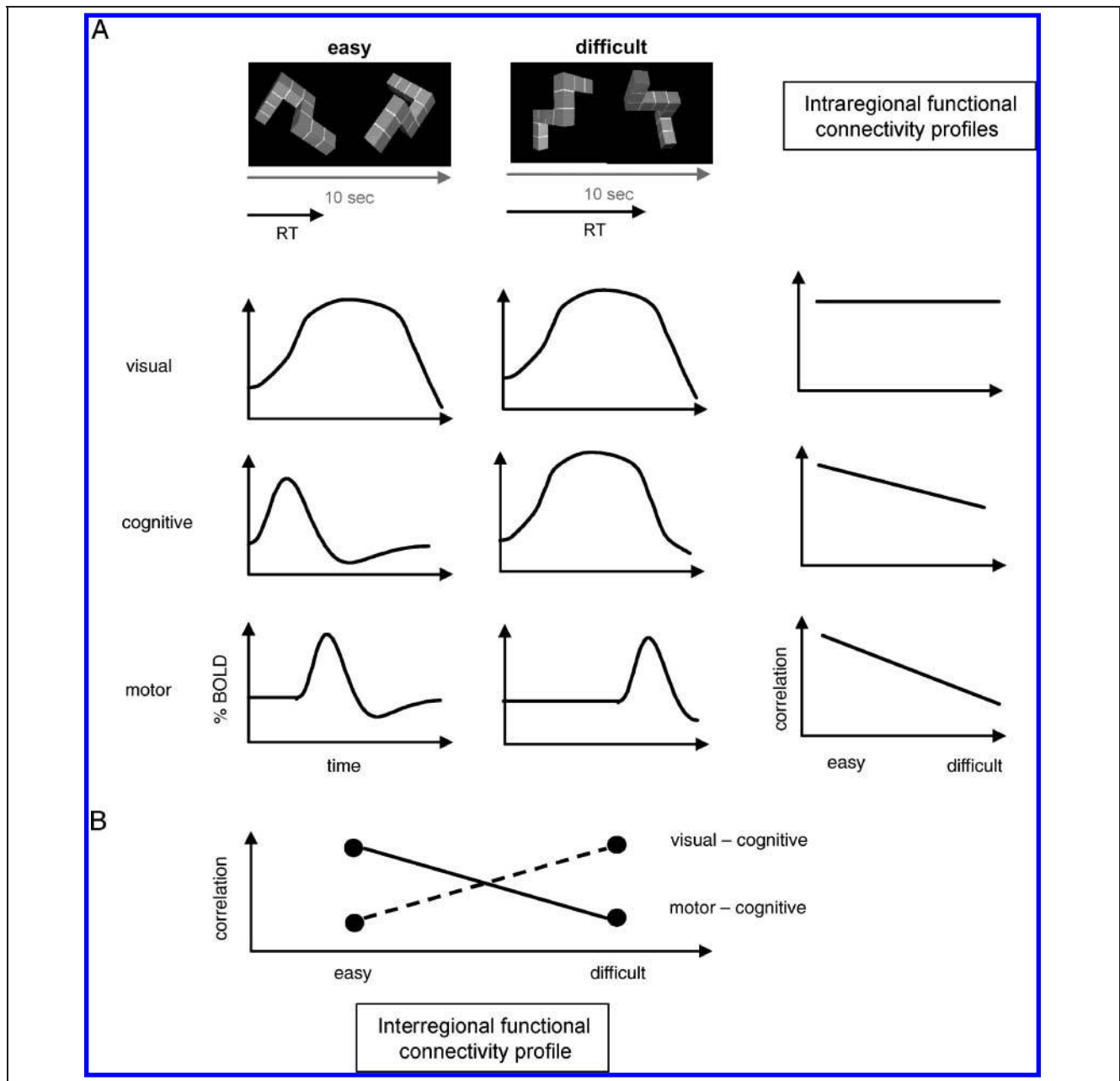


Figure 2. Hypothetical experimental design for the investigation of connectivity using time-resolved fMRI. (A) Expected HRFs in three components (visual, cognitive, motor) of the rotation network at two levels of task difficulty. In the cognitive component, the FWHM increases with RTs, whereas the FWHM of the visual component roughly corresponds to the stimulus duration (10 sec). In addition, there should be a delayed onset of the HRF in the motor component. (B) Intraregional connectivity profiles resulting from the zero-order correlations between the HRFs in both task conditions. Although there is no decay in correlation in the visual component, a decrease in the cognitive and in the motor component is expected. (C) Interregional connectivity profiles resulting from the zero-order correlations between the HRFs in different nodes of the network.

MRI images using gradient-echo, echo-planar sequence (TR = 2 sec, TE = 40 msec, theta = 80°, in-plane resolution = 3.75 mm, interslice gap = 0.5 mm). Each functional image comprised 25 contiguous, 5-mm-thick axial slices to cover the whole brain. In addition, an inversion recovery EPI dataset was acquired at 43 near-axial 3-mm-thick planes parallel to the AC–PC line: TE = 73 msec, TI (inversion time) = 180 msec, TR = 16 sec, in-plane resolution = 1.72 mm, interslice gap = 0.3 mm.

Functional Activation Mapping

Data were first realigned and smoothed using a Gaussian filter (FWHM = 7.2 mm). Neural responses to the experimental design were determined by time-series analysis using gamma variate functions (peak responses at 4 and 8 sec) to give the best-fit (least-squares) model of the time series of the BOLD response at each intracerebral voxel. A goodness-of-fit statistic, the sum of

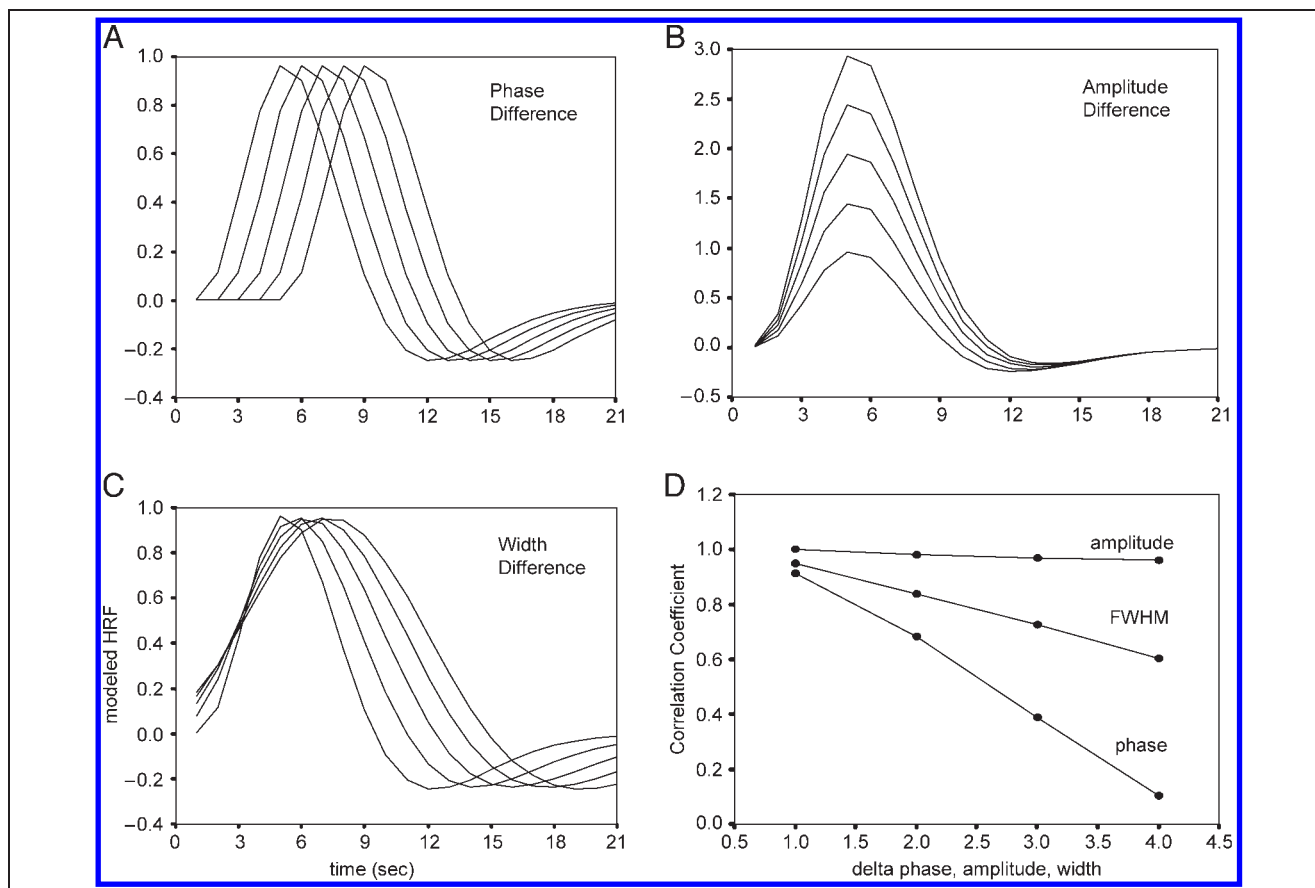


Figure 3. Changes in the zero-order correlation coefficient between models of the HR during event-related design. Functions varying in phase (A), amplitude (B), and width (C) were generated and the zero-order correlation coefficient between the initial model and each subsequent function were calculated for each altered parameter. (D) The expected change in correlation coefficients as a function of differences in amplitudes (red line), width (blue line), and phase shift (green line).

squares (SSQ) ratio, was then computed at each voxel. This was the ratio of the sum of squares of deviations from the mean intensity value due to the model (fitted time series) divided by the sum of squares due to the residuals (original time series minus model time series). To sample the distribution of SSQ ratio under the null hypothesis that observed values of SSQ ratio not determined by experimental design (with minimal assumptions), the time series at each voxel was permuted using a wavelet-based resampling method (Bullmore et al., 1999, 2001). Observed and randomized SSQ ratio maps were transformed into the standard space of Talairach and Tournoux (1988) as outlined in Brammer et al. (1997). Prior to transformation, a Talairach target image was computed by transforming 20 local structural images into standard space using explicit landmark identification. The fMRI data are then transformed onto the template in two stages. Initially, the fMRI data are rescaled to the same voxel dimensions as the structural image and then registered using a rigid body transformation. Subsequently, the transformed fMRI data are registered to the template image using an affine transform. Once these two transforms have been computed, the SSQ ratio maps as well as the observed SSQ maps in

native space can be transformed into Talairach space by subjecting them to the same transformation steps. A group brain activation map was produced for each experimental condition by testing the median observed SSQ ratio over all subjects (median values were used to minimize outlier effects) at each voxel in standard space against a critical value of the permutation distribution for median SSQ ratio ascertained from the spatially transformed wavelet-permuted data.

Time Series Extraction and Concatenation of the Condition-specific Eigentimeseries

Subsequent to functional activation mapping, a set of 6 regional time series was extracted. This included the five regions specified in the Jordan model (i.e., OC, ITP, DE, PP, PMd), as well as the primary motor cortex. Because subjects performed the button press with their right hand, significant functional activation in the primary motor cortex was observed in the left hemisphere exclusively. Therefore, the path analysis was restricted to ROIs in the left hemisphere. Time series were extracted from the motion-corrected images for individual subjects as average signal intensities in a significantly activated cluster

of voxels in 3-D space. This was performed using an automated procedure, which identified the native $\{x, y, z\}$ coordinates corresponding to the significantly activated voxels in the generic activation map.

Initially, each regional time series consisted of 760 data points collected across the whole experimental run. The first and last 60 data points were acquired during resting state and were disregarded. The remaining 640 data points consisted of volumes acquired during the four experimental conditions. As demonstrated in Figure 3, the segments of signal corresponding to the presentation of each of the four activation conditions were concatenated, resulting in a set of four task-specific or within-task time series for each region (Honey et al., 2003; Horwitz, Deiber, Ibanez, Sadato, & Hallett, 2000). For each condition, 20 trials were presented at an ISI of 16 sec (8 data points per trial at TR of 2 sec). Thus, each of the four within-task time series consisted of 160 data points. For each region i ($i = 1, \dots, 6$) and each condition j ($j = 1, \dots, 4$), this raw data matrix was denoted as \mathbf{X}_{ij} with the dimensions ($n = 160 \times p = 10$), where n denotes the number of data points per condition and p is equal to the number of subjects. The columns of this matrix were standardized to zero mean and unit variance.

In order to identify an average pattern of response, \mathbf{X}_{ij} was subject to principal component analysis (Bullmore et al., 2000; Buchel, Coull, & Friston, 1999; Fletcher, Buchel, Josephs, Friston, & Dolan, 1999). Initially, singular value decomposition was applied to \mathbf{X}_{ij} ($\mathbf{X} = \mathbf{U}\mathbf{\Delta}\mathbf{W}^T$) to find r eigenvectors $\mathbf{W}_{(p \times r)}$ as well as their associated eigenvalues $\mathbf{\Lambda}_{(r \times r)}$. Multiplying \mathbf{W} by $\mathbf{\Lambda}^{-1}$ resulted in the matrix of factor score coefficients $\mathbf{B}_{(p \times r)}$. The matrix of factor score coefficients $\mathbf{F}_{(n \times r)}$ containing the eigentime-series of \mathbf{X}_{ij} was then computed as the product of \mathbf{X}_{ij} and \mathbf{B} . Only the first eigentime-series of \mathbf{X}_{ij} was retained, which constituted a single representative for the activation in a particular region i and a specific condition j across subjects. In the final step, a data matrix \mathbf{D}_j , with the dimensions ($n \times i$), was computed for each condition j . The covariance matrix \mathbf{S}_j of \mathbf{D}_j with $\mathbf{S}_j \propto \mathbf{D}_j^T \mathbf{D}_j$ was the subject to path analysis. Because time series were standardized, \mathbf{S}_j was equal to the correlation matrix. Details of the time-resolved analysis can be found elsewhere (Ecker et al., 2006). This analysis basically consisted of identifying the FWHM of the HRFs in each region and rotation condition. Subsequently, the FWHM was correlated with RTs.

Intraregional Functional Connectivity Profiles

In order to examine whether changes in temporal characteristics of the HRF are reflected in zero-order correlation coefficients, interregional connectivity profiles were created. These connectivity profiles indicate how much the temporal parameters of the HRF within a particular region changes with the level of task difficulty. The basic idea behind this approach is summarized in Figure 3. The intraregional connectivity profiles across

experimental conditions were created in the following manner. For each ROI, the HR (extracted from the first eigentime-series) during 0° rotation was correlated with the hemodynamic response in the 20° , 60° , and 100° rotation condition, for instance, $r(\text{HRF}_{\text{cond } 0^\circ}, \text{HRF}_{\text{cond } 20^\circ})$, $r(\text{HRF}_{\text{cond } 0^\circ}, \text{HRF}_{\text{cond } 60^\circ})$, $r(\text{HRF}_{\text{cond } 0^\circ}, \text{HRF}_{\text{cond } 100^\circ})$. Subsequently, the decrease in the zero-order correlation coefficient between the HRF during 20° and 100° rotation conditions was calculated for each ROI and the resulting data were sorted in a descending order. Ultimately, no decay in zero-order correlation indicates that the temporal parameters of the HRF in a particular region do not change with the level of task difficulty. ROIs might therefore be allocated to clusters depending on the decay in correlation coefficient across rotation conditions.

Structural Equation Modeling

Specification of the Neuroanatomical Model and Estimation of Residual Variances

Three neuroanatomical models were investigated in this investigation: (1) the neuroanatomical model employed postulated for female subjects by Jordan et al. (2002), (2) an extended version of Jordan's original model, and (3) a model with feed-backward connections. This extended network included activation in M1 as an additional ROI, which was assumed to receive input from the PMd. The path diagram of the extended Jordan model is shown in Figure 1A. The model comprises five endogenous ROIs (i.e., ROIs receiving afferent input), one exogenous ROI (i.e., ROI with efferent connections exclusively), five effective connections (i.e., direct paths), and one covariance. The structural equations underlying the path diagram in Figure 1A can be formalized as:

$$\mathbf{y}_{(5 \times 1)} = \mathbf{B}_{(5 \times 5)} \mathbf{y}_{(5 \times 1)} + \mathbf{\Gamma}_{(5 \times 1)} \mathbf{x}_{(1 \times 1)} + \boldsymbol{\zeta}_{(5 \times 1)},$$

where \mathbf{y} is a vector of the endogenous ROIs, \mathbf{x} is a vector of the exogenous ROIs, \mathbf{B} is a matrix of path coefficients for endogenous ROIs, $\mathbf{\Gamma}$ contains path coefficients for exogenous ROIs, and $\boldsymbol{\zeta}$ is a vector of errors. This equation can be rewritten to:

$$\begin{bmatrix} \text{ITp} \\ \text{DE} \\ \text{PP} \\ \text{PMd} \\ \text{M1} \end{bmatrix} = \begin{bmatrix} 0 & 0 & 0 & 0 & 0 \\ 0 & 0 & 0 & 0 & 0 \\ 0 & \beta_{32} & 0 & 0 & 0 \\ 0 & 0 & \beta_{43} & 0 & 0 \\ 0 & 0 & 0 & \beta_{54} & 0 \end{bmatrix} \begin{bmatrix} \text{ITp} \\ \text{DE} \\ \text{PP} \\ \text{PMd} \\ \text{M1} \end{bmatrix} + \begin{bmatrix} \gamma_1 \\ \gamma_2 \\ 0 \\ 0 \\ 0 \end{bmatrix} [\text{IOC}] + \begin{bmatrix} \zeta_1 \\ \zeta_2 \\ \zeta_3 \\ \zeta_4 \\ \zeta_5 \end{bmatrix}.$$

Two additional matrices were specified. The first one is the covariance matrix of \mathbf{x} conventionally denoted as $\Phi_{(p \times p)}$ with $\Phi = \mathbf{E}(\mathbf{xx}^T)$. Because the model contained only one exogenous variable, Φ contained a single element, ϕ_{11} , which is the variance of IOC. The second

one is the matrix of the residuals for each endogenous variable conventionally denoted as $\Psi_{(q \times q)}$ with $\Psi = (\zeta\zeta^T)$. The residual variances of each ROI receiving hypothesized projections were estimated a priori. Instead of fixing the residual variances at an arbitrary value, these were estimated by the ratio between the first eigenvalue and the sum of eigenvalues (Bullmore et al., 2000) with

$$\psi_i = 1 - \frac{\lambda_1^2}{\sum_{j=1}^m \lambda_j^2}.$$

Because eigentimeseries were standardized variables with unit variance, the sum of the eigenvalues equals the number of ROIs in the model. Apart from the residual variances in each ROI, the model postulates correlated residuals between ITP and DE, indicated by a two-headed arrow. The elements ψ_{12} and ψ_{21} of Ψ are therefore nonzero and equal, whereas all other non-diagonal elements of Ψ were zero. Ψ was formalized as:

$$\Psi = \begin{bmatrix} * \Psi_{11} & \Psi_{12} & 0 & 0 \\ \Psi_{21} & * \Psi_{22} & 0 & 0 \\ 0 & 0 & * \Psi_{33} & 0 \\ 0 & 0 & 0 & * \Psi_{44} \end{bmatrix}.$$

The residual variances that were estimated using principal component analysis are marked with an asterisk.

The model with feedback connections included a backward connection from the PMd to PP, and connections from the PP to DE and ITP. This model is displayed in Figure 1B.

Assessment of Normality

Most commonly used fitting functions in SEM (e.g., F_{ML} , F_{GLS}) derive from the assumption of a multinormal distribution of the observed variables, although F_{ML} and F_{GLS} are generally also justified when the distribution of the observed variables has no excess kurtosis. Prior to parameter estimation, indicator variables were therefore tested for multivariate normality, which was assessed on the basis of the critical ratio (CR) for the kurtosis and skewness of each indicator variable. The kurtosis of all variables exhibited a CR larger than +2.0 or smaller than -2.0, thus indicating approximate normal distribution. In addition, Mardia's measure of multivariate kurtosis (Mardia, 1974) was inspected with a CR exceeding a value of 1.96, indicating severe nonnormality. Mardia's coefficient for the included observed variables was within generally accepted limits and multinormal could be established. Maximum likelihood estimation (F_{ML}) was

therefore justified and employed for model fitting. Because the below specified models were subsequently fitted for each condition separately, normality assessment was carried out for each condition-specific, concatenated eigentimeseries. The normality assessment was carried out using AMOS 5.0.1.

Model Identification

The identified parameters in a path model are the elements of Σ , which denotes the population covariance matrix of \mathbf{y} and \mathbf{x} . A covariance matrix for p variables has $(1/2)p(p + 1)$ nonredundant elements. The extended Jordan model thus consisted of 21 known parameters and 15 free parameters for the original model. The parameters whose identification status is unknown are in θ , which θ contains the t free and (nonredundant) constrained parameters of \mathbf{B} , Γ , Φ and Ψ . As indicated above, there were three free parameters in \mathbf{B} and two parameters in Γ . Additionally, there was one free residual variance ψ_{21} and the covariance of IOC, ϕ_{11} . The total number of free, nonredundant parameters in θ was 7. Thus, the number of estimable parameters in the model was smaller than the number of data points and the model was overidentified. The so-called *t-rule*, which offers a necessary but not sufficient condition of identification was thus satisfied with:

$$t \leq (1/2)(p + q)(p + q + 1)$$

with $7 \leq 15$ being true.

Estimation of Structural Parameters and Model Fitting

The unknown parameters in \mathbf{B} , Γ , Φ , and Ψ were estimated so that the predicted covariance matrix indicated by the model (i.e., Σ) was close to the sample covariance matrix \mathbf{S} . Σ is obtained by substituting estimates of θ , $\hat{\theta}$, in $\Sigma(\theta)$ so that $\Sigma = \Sigma(\hat{\theta})$. In order to reduce the discrepancy between each element in Σ and that in \mathbf{S} , a fitting function $F(\mathbf{S}, \Sigma(\hat{\theta}))$ was minimized in an iterative fashion using a maximum-likelihood (ML) fitting approach. The asymptotic distribution of the F_{ML} estimators multiplied by $(N - 1)$, is an approximation of a χ^2 distribution with $0.5(p + q)(p + q + 1) - t$ degrees of freedom. Here, N equals the sample size, t is the number of free parameters, and F_{ML} is the value of the fitting function evaluated at the final estimates. Under the null hypothesis of $H_0: \Sigma = \Sigma(\hat{\theta})$, the χ^2 parameter provides a goodness-of-fit index of the overall model.

Assessment of Model Fit and Model Comparison

The overall goodness of each model was assessed using multiple fit indices commonly used in SEM. The adjusted

goodness of fit index (AGFI) was examined to identify the absolute model fit requiring values of $> .9$ to denote acceptable model fits (Bentler & Bonett, 1980). The root mean square error of approximation (RMSEA) (Steiger, 1990) was used to assess the discrepancies between the observed and implied variance-covariance matrix. In general, RMSEAs smaller than .05 indicate a close approximation fit, values between .05 and .08 suggest a reasonable approximation fit, and values larger than .1 denote a poor fit (Kline, 1998). Finally, two comparative fit indices—the comparative fit index (CFI) and the normed fit index (NFI) (Bentler & Bonett, 1980)—were used to compare the performance of the specified models to the performance of a baseline (null or independence) model. Here, values $> .9$ were considered to be consistent with a good model fit (Bentler & Bonett, 1980).

To examine changes in effective connections across different levels of task difficulties, several alternative models were compared. The variant and invariant direct paths in the extended Jordan model were identified using the nested or stacked model approach (McIntosh & Gonzalez-Lima, 1994). Initially, a model in which all path coefficients were constrained to be equal across the 0° and 100° rotation condition (null model) was compared with a model in which all coefficients were allowed to differ between conditions (alternative model). If the model with variable paths indicated a significant improvement in model fit, further analysis was carried out to determine the specific effective connections varying significantly across conditions. In order to accomplish this, the null model was compared with a model in which a particular path was allowed to vary across conditions. If the fit index of this model improved significantly ($p(\Delta\chi^2) < 0.05$) in comparison to the null model, it was concluded that this particular path varied between

the 0° and 100° rotation condition. This procedure was carried out repeatedly by allowing a different path coefficient to vary across conditions. In the stacked-model analysis, the residual influences were estimated. Their path coefficients, however, were constrained to be unity in order to reduce the number of estimated parameters (McIntosh & Gonzalez-Lima, 1994). The variance estimates resulting from the initial 0° rotation were kept constant in the 100° rotation condition. Finally, the model with feedback connections was compared with the extended serial model.

RESULTS

Functional Activations in ROIs and Results of the Time-resolved fMRI Analysis

The main foci of significant brain activation for the female subject group and a full description of the time-resolved fMRI analysis results can be found elsewhere (Ecker et al., 2006). Significant functional activation was observed in all ROIs specified by the Jordan model. These included (1) several areas of the visual system such as early visual areas in the occipital lobe (OC or BA 17/18), dorsal extrastriate visual areas (DE) corresponding to BA 19/39, and activation in the posterior inferior temporal lobe (ITp or BA 19/37); (2) regions of the motor system such as the dorsal premotor cortex (PMd or lateral BA 6) and the primary motor cortex (M1 or BA 4); and (3) activation in the parietal lobe including superior and inferior regions (BA 39/40/7). Talairach coordinates and statistical test parameters for these ROIs are listed in Table 1.

Furthermore, we have previously demonstrated that the temporal characteristics of the HRF in visual regions

Table 1. Main Foci of Group Brain Activation for 10 Female Subjects during Performance of the Mental Rotation Task

<i>Region Definition</i>	<i>Hemisphere</i>	<i>Tal (x, y, z)</i>	<i>SSQ Ratio</i>	<i>p</i>	<i>Effect Size (%)</i>
M1	L	−36, −22, 48	0.025	3×10^{-6}	–
PMd-proper	R	32, −11, 48	0.018	3×10^{-6}	0.192
PMd-proper	L	−22, −11, 48	0.025	3×10^{-6}	0.218
OC	M	−11, −67, −2	0.018	3×10^{-6}	0.247
ITp	R	43, −59, −13	0.037	3×10^{-6}	0.273
ITp	L	−40, −70, −7	0.015	2×10^{-5}	0.296
DE	L	−22, −70, 20	0.036	3×10^{-6}	0.279
DE	R	29, −63, 20	0.019	3×10^{-6}	0.252
Parietal ROI	L	−22, −63, 31	0.015	2.6×10^{-5}	0.197
Parietal ROI	R	29, −56, 31	0.012	1.4×10^{-4}	0.219

Contrast indicates the contrast map with the largest fit indices for a particular ROI.

L = left; R = right; M = medial; M1 = primary motor cortex; PMd = premotor cortex; ITp = posterior inferior temporal lobe; DE = dorsal extrastriate visual areas; OC = occipital cortex.

do not change significantly across levels of task difficulty (Ecker et al., 2006). Instead, HRFs were constantly elevated for a time roughly equal to the stimulus duration ($\sim 9 \pm 1$ sec). These findings lead us to the conclusion that visual regions do not actively participate in the mental spatial transformation but rather represent processes involved in visual perception. The FWHM in the left parietal ROI and in the left PMd-proper, however, did increase with RTs, thus suggesting that these regions are involved in the rotational process itself. There was no significant change of the FWHM with RTs in the primary motor cortex. Here, the mean FWHM across all four rotation conditions was 4.74 sec. The results of the time-resolved analysis for the selected ROIs are listed in Table 2.

Intraregional Functional Connectivity Profiles across Experimental Conditions

The interregional connectivity profiles for the selected ROIs are displayed in Figure 4. Overall, the observed profiles behave in a similar fashion as the expected profiles in Figure 2. The slope of these profiles indicates how much the temporal characteristics of the HRF during 20°, 60°, and 100° rotation change in comparison to the 0° rotation. As can be seen in Figure 5, the intraregional functional connectivity could indeed be manipulated by alternating angular disparities. As would be expected on the basis of the time-resolved analysis, the decay in intraregional connectivity was largest in the parietal ROI, in the PMd, and in M1. In the parietal ROI, the correlation coefficient decreased from .872 correlating 0° with 20° rotation to .668 correlating 0° with 100° rotation ($\Delta r = .204$). These findings imply that either width or latency of the response in these regions changes with the level of task difficulty. As can be further

seen in Figure 5, the decrease in correlation was minimal in regions of the visual system (i.e., ITp and DE). The decrease was at its lowest in the ITp when the correlation dropped from .948 comparing 0° with 20° rotation, to .918 correlating 0° with 100° rotation ($\Delta r = .03$). One can therefore conclude that the processing load minimally affects the temporal characteristics of the HRF in the ITp and DE, which further suggests that these regions do not actively participate in the computation of the mental transformation, which has been proposed previously (Ecker et al., 2006).

Absolute Fit of the Jordan Model and the Extended Jordan Model

Initially, the hypothesized models were fitted separately for each level of task difficulty in order to assess the absolute model goodness. The input matrices to the path analysis were the covariance matrices of the concatenated first eigentimeseries for ROIs in the left hemisphere, which are listed in Table 3. All interregional correlation coefficients were significant on $p < .05$, thus indicating a high degree of functional connectivity among the selected ROIs. Table 3 further shows the residual variances for each ROI that were estimated on the basis of the principal component analysis.

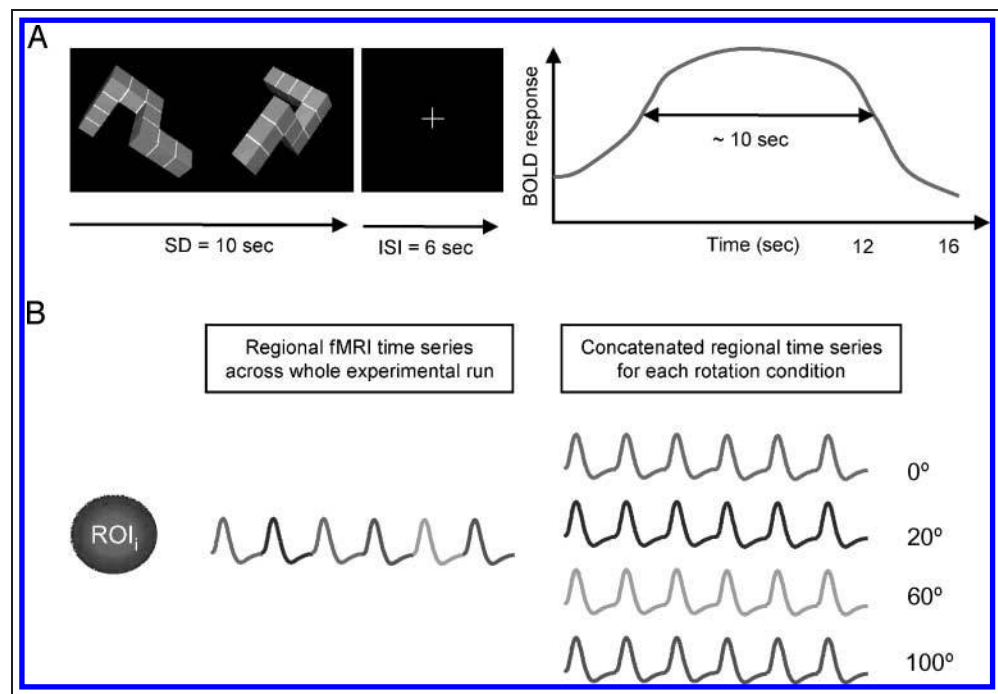
The estimated path coefficients as well as the absolute fit indices for the Jordan model and the extended Jordan model are summarized in Tables 4 and 5. Overall, both networks did not provide an adequate fit to the observed interregional correlation matrix although all path coefficients were highly significant at $p < .01$. In all rotation conditions, the χ^2 parameters were significant at a type I error probability of 5%, thus suggesting a significant discrepancy between the correlation matrix

Table 2. Correlations between Subject's Reaction Time Measures and Parameters of the Hemodynamic Response in ROIs during Performance of the Mental Rotation Task

Region Definition	Hemisphere	Amplitudes		FWHM	
		Correlation with RTs	<i>p</i>	Correlation with RTs	<i>p</i>
M1	L	-.129	< .5	.226	< .2
PMd-proper	R	.378	< .1	.559*	< .01
PMd-proper	L	.365	< .1	.487*	< .05
OC	M	-.221	< .3	-.04	< .9
ITp	L	.22	< .3	.139	< .5
ITp	R	–	–	–	–
DE	L	.217	< .3	.03	< .9
DE	R	.117	< .7	-.125	< .7
Parietal ROI	L	.526*	< .01	.399*	.05
Parietal ROI	R	.301	< .2	.196	< .5

*Significant correlations ($p < .05$).

Figure 4. Intraregional functional connectivity profiles across experimental conditions resulting from the HRF extracted from the first eigentimeseries. (A) Zero-order Pearson correlation coefficients between the HRF in the 0° rotation condition and the HRF in each of the subsequent conditions for the selected ROIs. (B) Decrease in correlation across conditions for each ROI sorted in descending order. The largest decrease was observed in ROIs whose FWHM of the HRF increase with RTs (e.g., PP, PMd). The slope of the profile was smallest in ROIs whose temporal parameters of the HRF were constant across conditions (e.g., DE, ITp).



predicted by the model and the population correlation matrix. In the Jordan model, this discrepancy was largest in the 100° rotation condition ($\chi^2(9) = 83.68, p < .001$) and lowest in the 20° rotation condition ($\chi^2(9) = 59.37, p < .001$). In the 60° rotation condition, the correlation matrix was not positive definite and path coefficients could not be estimated. Large discrepancies between the model and the observed data were also indicated by the RMSEA, which should be below .1 to indicate a good fit to the data (Steiger, 1990). In this study, however, all RMSEAs were larger than .18, which was the RMSEA observed at 20° angular disparity. In addition, all remaining fit indices converge in suggesting a general lack of fit. Similar results were found in the extended Jordan model. Here, the χ^2 parameter was also lowest in the 20° condition ($\chi^2(14) = 88.36, p < .001$) and highest in the 100° rotation condition ($\chi^2(14) = 95.55, p < .001$). The lowest RMSEA was observed in the 20° (RMSEA = 0.18), indicating a “poor fit” (Kline, 1998).

Changes in Effective Connections across Levels of Task Difficulty

To ascertain whether the level of task demand induces changes in connectivity within the neurocognitive network underlying mental rotation, the effective connections specified by the extended Jordan model were examined during the lowest and highest levels of task difficulty (i.e., 0° and 100° rotation). Initially, a model in which all path coefficients were constrained to be equal across the 0° and 100° rotation condition was compared with a model in which all paths were allowed to vary across conditions. As shown in Table 6, the nested model

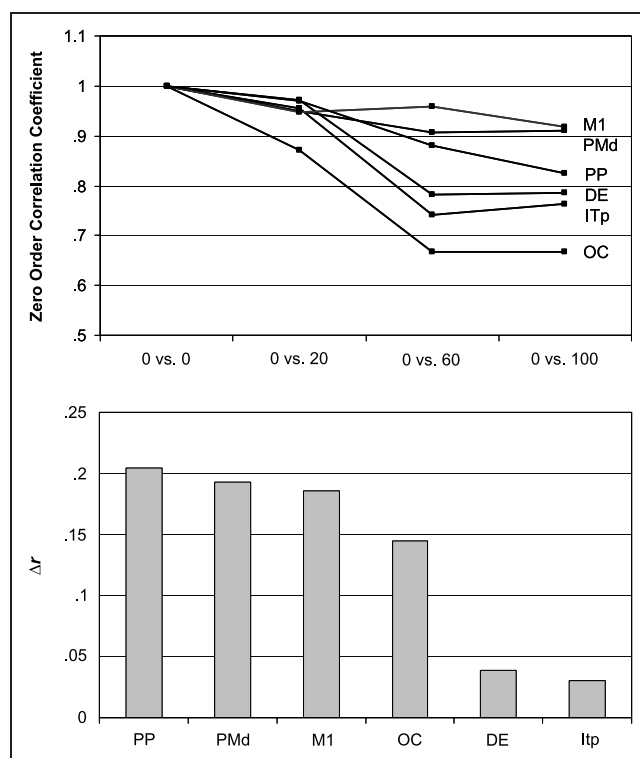


Figure 5. (A) Display and timings of individual events. In all condition stimuli were presented for 10 sec, followed by 6 sec fixation cross, after which the hemodynamic response (HRF) should have decayed to baseline level. Because there is no overlap between HRFs, a condition-specific time series representing signal intensities acquired during a particular trial condition exclusively can be concatenated (B).

Table 3. Variance–Covariance Matrix of the Concatenated First Eigentimeseries for ROIs in the Left Hemisphere ($n = 160$)

	<i>M1</i>	<i>PMd</i>	<i>DE</i>	<i>PP</i>	<i>ITp</i>	<i>OC</i>
0°						
M1	1.00					
PMd	.823*	1.00				
DE	.687*	.668*	1.00			
PP	.755*	.818*	.694*	1.00		
ITp	.691*	.674*	.746*	.705*	1.00	
OC	.646*	.584*	.529*	.525*	.500*	1.00
ψ	.634	.732	.783	.766	.769	.821
20°						
M1	1.00					
PMd	.684*	1.00				
DE	.653*	.721*	1.00			
PP	.622*	.755*	.850*	1.00		
ITp	.554*	.645*	.760*	.712*	1.00	
OC	.487*	.297*	.229*	.231*	.291*	1.00
ψ	.740	.741	.752	.737	.759	.851
60°						
M1	1.00					
PMd	.715*	1.00				
DE	.704*	.841*	1.00			
PP	.701*	.845*	.853*	1.00		
ITp	.693*	.837*	.861*	.829*	1.00	
OC	.378*	.447*	.386*	.320*	.354*	1.00
ψ	.791	.689	.711	.698	.696	.833
100°						
M1	1.00					
PMd	.609*	1.00				
DE	.610*	.851*	1.00			
PP	.599*	.829*	.854*	1.00		
ITp	.569*	.813*	.869*	.848*	1.00	
OC	.499*	.556*	.584*	.496*	.540*	1.00
ψ	.824	.714	.695	.676	.702	.833

(m) = medial, ψ = residual variance.

*Correlation is significant at the .01 level (two-tailed).

analysis revealed that the model with variant paths provided a significant improvement in model fit as compared to the model with invariant paths ($\Delta\chi^2(6) = 38.15$, $p < .001$). This result demonstrates that the level of task difficulty induces changes in interregional connections overall. To further examine which paths change significantly across conditions, a model in which a specific path was allowed to vary was compared to the model with invariant paths. Only two out of the five path coefficients changed significantly across conditions: (1) the path coefficient between DE and PP increased significantly by 0.16 from 0° rotation to 100° rotation ($\Delta\chi^2(1) = 4.26$, $p < .01$); (2) the path coefficient between PMd and M1 decreased significantly by 0.31 from 0° rotation to 100° rotation ($\Delta\chi^2(1) = 14.29$, $p < .01$). All other path coefficients were constant across conditions.

Comparison of the Serial Models with the Parallel Model

The final part of the analysis aimed to compare the serial networks with the feed-backward network displayed in Figure 1B. The estimated path coefficients and the absolute fit indices of this model are summarized in Table 7. Interestingly, the feed-backward model provided a better fit than the serial models during 20° and 100° rotation, but not in the 0° rotation condition. During 0° rotation, the parallel model fitted significantly worse than the Jordan model ($\Delta\chi^2 = 61.14$, $p < .001$) and the extended model ($\Delta\chi^2 = 10.7$, $p < .01$). During 20° , the parallel model improved the goodness of fit as compared to the Jordan model ($\Delta\chi^2 = 3.43$, $p < .2$) and the extended Jordan model ($\Delta\chi^2 = 32.41$, $p < .001$). In the 100° rotation condition, the parallel model improved the goodness of fit as compared to the Jordan model by $\Delta\chi^2 = 8.35$ ($p < .01$) and by $\Delta\chi^2 = 20.22$ ($p < .001$) as compared to the extended model. The improvement of fit, hence, seems to be rotation specific as it was not observed in the control conditions providing further evidence for the hypothesis that mental rotation requires parallel rather than serial information processing.

DISCUSSION

The main aim of this study was to investigate the validity of the sequentially organized rotation network originally proposed by Jordan et al. (2002), and to examine changes in effective connections across different levels of task difficulty. Path analysis was combined with a time-resolved fMRI analysis to relate the results on the network level to specific changes in the temporal characteristics of the HRF on the level of individual network nodes. Finally, we have shown that a model with feedback connections provided a significantly better fit than the sequential models.

It was firstly demonstrated that the proposed model did not provide an adequate fit to the data overall,

Table 4. Estimated (Un)standardized Path Coefficients for the Neuroanatomical Network Underlying MR as Suggested by Jordan et al. (2002)

	0°			20°			60°			100°		
	<i>b</i>	β	<i>t</i>	<i>b</i>	β	<i>t</i>	<i>b</i>	β	<i>t</i>	<i>b</i>	β	<i>t</i>
<i>Path Connections</i>												
OC → DE	0.53	0.51	7.51*	0.23	0.26	3.32*				0.50	0.51	7.48*
OC → ITp	0.50	0.50	7.17*	0.29	0.32	4.20*				0.54	0.54	8.10*
DE → PP	0.69	0.63	10.28*	0.85	0.55	11.16*				0.85	0.69	11.88*
PP → PMd	0.82	0.73	13.58*	0.75	0.71	12.55*				0.83	0.74	13.84*
DE ↔ ITp	0.52	0.50	18.32*	0.53	0.64	20.97*				0.57	0.59	39.26*
<i>Fit Indices</i>												
χ^2 (<i>df</i> = 9)		59.53			59.37			n/a			83.68	
RMSEA		.19			.188			n/a			.229	
AGFI		.68			.71			n/a			.520	
CFI		.85			.83			n/a			.76	
NFI		.84			.82			n/a			.76	
PGFI		.48			.50			n/a			.43	

b = unstandardized path coefficient; β = standardized path coefficient; *t* = statistical test parameter associated with each path coefficient; RMSEA = root mean squared error of approximation (Steiger, 1990); AGFI = adjusted goodness-of-fit index; CFI = comparative fit index (Bentler, 1980); NFI = normed fit index (Bentler & Bonett, 1980); PGFI = parsimony goodness-of-fit index (James, Mulaik, & Brett, 1982); n/a = correlation matrix not positive definite.

*Significant at $p < .01$.

despite reproducing the interregional covariance matrix significantly better than the independence model or null model. This suggests that although all nodes within the network interact during task performance to a high degree, the causal structure of the model does not adequately represent the cortical interactions within the rotation network. The Jordan model is essentially a feed-forward model in which sequential information processing prevails. It therefore conforms to traditional cognitive models describing the complex cognitive process underlying mental rotation by a set of functionally distinct processing stages. These include (1) perceptual encoding, (2) identification/discrimination of the presented object and its orientation, (3) mental rotation itself, (4) judgment of parity, (5) response selection, and (6) response execution. These stages are assumed to be organized sequentially with discrete transmission of information from one stage to the next, mainly because RTs increase linearly with the degree of angular disparity (Corballis, 1988; Shepard & Cooper, 1982). The lack of fit of the Jordan model thus challenges the feed-forward sequential nature of the cognitive process underlying mental rotation. Instead, it seems to point toward more recent cognitive theories suggesting that certain sub-processes occur in parallel with the mental rotation stage (Farah, 1995; Kosslyn, Maljkovic, Hamilton, Horwitz, & Thompson, 1995). There is also some empirical evidence

coming from psychological studies and EEG studies that consecutive stages do, indeed, overlap (Heil, Rauch, & Hennighausen, 1998; Ruthruff & Miller, 1995).

Indirect evidence for parallel processing within the network can also be found by means of the variance-covariance matrix. In a discrete or serial network, one network component transmits its output in a single distinct message to the subsequent state. Assuming that Region A projects to Region C via Region B (i.e., $A \rightarrow B \rightarrow C$), there should be a partial overlap between A and B, as well as between B and C. Little or no overlap on the other hand would be expected between A and C. On the basis of the models in Figure 3, the expected correlation coefficient following an increase in RT of approx. 3 sec from 1.7 sec at 0° to 4.7 sec at 100° rotation (Ecker et al., 2006) is approximately 0.4. In the serial Jordan model, DE is hypothesized to project to PP which, in turn, projects to PMd. From a theoretical perspective, one would thus expect a correlation coefficient $< .4$ between these regions. The correlation matrix, however, indicates that the interregional correlations between these regions were highly significant in all conditions with the lowest coefficient of $r_{(DE, PP)} = .694$ at 0° and $r_{(PP, PMd)} = .755$ at 20° rotation. It is therefore unlikely that the rotation network operates in a strictly serial fashion.

A second reason for the general lack of model fit might be that the postulated model is incomplete in

Table 5. Estimated (Un)standardized Path Coefficients for the Neuroanatomical Network Underlying MR as Suggested by the Extended Jordan Model

	0°			20°			60°			100°		
	b	β	t	b	β	t	b	β	t	b	β	t
<i>Path Connections</i>												
OC \rightarrow DE	0.53	0.51	7.51*	0.23	0.26	3.32*				0.50	0.51	7.48*
OC \rightarrow ITp	0.50	0.50	7.17*	0.29	0.32	4.20*				0.54	0.54	8.10*
DE \rightarrow PP	0.69	0.63	10.28*	0.85	0.55	11.16*				0.85	0.69	11.88*
PP \rightarrow PMd	0.82	0.73	13.58*	0.75	0.71	12.55*				0.83	0.74	13.84*
DE \leftrightarrow ITp	0.52	0.50	18.32*	0.53	0.64	20.97*				0.57	0.59	39.26*
PMd \rightarrow M1	0.92	0.83	18.36*	0.68	0.70	12.21*				0.61	0.67	11.39*
<i>Fit Indices</i>												
χ^2 ($df = 14$)		109.97			88.36			n/a			95.55	
RMSEA		.21			.18			n/a			.19	
AGFI		.48			.67			n/a			.58	
CFI		.79			.83			n/a			.80	
NFI		.78			.81			n/a			.79	
PGFI		.43			.52			n/a			.48	

b = unstandardized path coefficient; β = standardized path coefficient; t = statistical test parameter associated with each path coefficient; RMSEA = root mean squared error of approximation (Steiger, 1990); AGFI = adjusted goodness-of-fit index; CFI = comparative fit index (Bentler, 1980); NFI = normed fit index (Bentler & Bonett, 1980); PGFI = parsimony goodness-of-fit index (James et al., 1982); n/a = correlation matrix not positive definite.

*Significant at $p < .01$.

terms of the included network components. Apart from the ROIs suggested by Jordan et al. (2002), several other regions have repeatedly been found to be activated by rotation paradigms. These mainly include additional motor regions such as the supplementary motor area or SMA-proper, the head of the caudate nucleus in the basal ganglia, as well as the ventral premotor cortex or PMv (Vingerhoets et al., 2002; Alivisatos & Petrides, 1997; Parsons et al., 1995). In addition, several studies have reported activation in the lateral occipital sulcus or LOS

(Shendan & Stern 2007; Gauthier, Hayward, & Tarr, 2002; Goebel, Linden, Lanfermann, Zanella, & Singer, 1998), in the ventrolateral prefrontal cortex, and in the parahippocampal place area (Shendan & Stern 2007). There is also evidence that the parietal cortex might be further parcellated into functionally different subdivisions (Podzebenko, Egan, & Watson, 2002).

The (in)exclusion of particular nodes naturally changes the specification of effective connections within the network. For instance, according to the Jordan model,

Table 6. Variant and Invariant Path Connections in the Extended Jordan Model

<i>Path Connection</i>	<i>Path Coefficient</i>		χ^2 Invariant ($df = 29$)	χ^2 Variant ($df = 28$)	$\Delta\chi^2$ ($df = 1$)
	0°	100°			
OC \rightarrow DE	0.53	0.50	252.09	252.68	0.59
OC \rightarrow ITp	0.50	0.54	252.09	252.69	-0.6
DE \rightarrow PP	0.69	0.85	252.09	247.83	4.26*
PP \rightarrow PMd	0.82	0.83	252.09	251.92	0.17
PMd \rightarrow M1	0.92	0.61	252.09	237.80	14.29*

χ^2 (in)variant = absolute fit index for the model with (in)variant path coefficients; $\Delta\chi^2$ = difference in absolute fit between the variant and invariant model.

*Significant at $p < .01$.

Table 7. Estimated (Un)standardized Path Coefficients for the Neuroanatomical Network with Feed-backwards Connections (see Figure 1B)

	0°			20°			60°			100°		
	b	β	t	b	β	t	b	β	t	b	β	t
<i>Path Connections</i>												
OC \rightarrow DE	-0.03	-0.02	-.37	0.19	0.18	2.68*				0.46	0.45	6.51*
OC \rightarrow ITp	0.02	0.02	0.27	0.23	0.22	3.34*				0.45	0.42	6.29*
DE \rightarrow PP	-0.62	-0.67	-7.98*	1.25	1.28	12.47*				1.76	1.85	15.49*
PP \rightarrow ITp	0.92	0.84	12.88*	0.24	0.23	3.36*				0.18	0.16	2.57*
PP \rightarrow DE	1.06	0.98	14.96*	0.18	0.18	2.85*				0.08	0.07	1.17*
PP \rightarrow PMd	0.24	0.23	3.59*	1.09	0.99	16.00*				1.24	1.07	17.19*
DE \leftrightarrow ITp	0.50	0.42	15.55*	0.50	0.46	15.85*				0.56	0.51	33.37*
PMd \rightarrow PP	1.10	1.14	10.94*	-0.68	-.74	-8.58*				-1.10	-1.27	-11.66*
PMd \rightarrow M1	0.92	0.77	15.05*	0.68	0.66	11.03*				0.61	0.60	9.36*
<i>Fit Indices</i>												
χ^2 ($df = 11$)		120.67			55.95			n/a			75.33	
RMSEA		.25			.00			n/a			.19	
AGFI		.43			.74			n/a			.67	
CFI		.80			.91			n/a			.92	
NFI		.79			.90			n/a			.91	
PGFI		.37			.45			n/a			.43	

b = unstandardized path coefficient; β = standardized path coefficient; t = statistical test parameter associated with each path coefficient; RMSEA = root mean squared error of approximation (Steiger, 1990); AGFI = adjusted goodness-of-fit index; CFI = comparative fit index (Bentler, 1980); NFI = normed fit index (Bentler & Bonett, 1980); PGFI = parsimony goodness-of-fit index (James et al., 1982); n/a = correlation matrix not positive definite.

*Significant at $p < .01$.

the posterior parietal cortex projects exclusively to the PMd and receives a projection from dorsal extrastriate visual areas. The posterior and inferior parietal cortex, however, receive projections from multiple sensory regions (i.e., visual, motor, and auditory) (Sakata & Kusunoki, 1992). Also, the Jordan model places particular emphasis on the parieto-occipital rather than the temporo-occipital pathway. The ventral processing stream might, however, play a major role in closing the stream of information processing from the visual system to the frontal premotor regions. From the ITp, information is transmitted to the temporal pole, which contains feed-forward connections to the frontal/prefrontal lobe, which, in turn, is extensively interconnected with the pre-SMA and the PMv (reviewed by Picard & Strick, 2001). In addition, the PMv is connected with the posterior-parietal lobe (Matelli, Luppino, & Rizzolatti, 1991).

A recent study by Shendan and Stern (2007) has also demonstrated a direct link between mental rotation and visual object categorization. Both processes seem to share a common network of prefrontal, dorsal, and ventral re-

gions of the posterior cortex, highlighting the general role of these regions in object cognition. Interestingly, there is evidence coming from ERP studies that the process of visual object categorization itself involves interactive, recurrent, and feedback processing in occipital and ventral temporal cortical regions (Shendan & Kutas, 2007). It has been suggested that object categorization requires three different stages: (1) early perceptual grouping indicated by P200, (2) matching the organized percept to stored visual knowledge reflected by N350, and (3) selection of a response between 500 and 850 msec. The matching phase (N350), which is an essential part of mental rotation, naturally requires reciprocal processing between memory contents and percepts.

Notably, the study by Shendan and Stern (2007) also highlights the importance of controlling for eye movements in order to dissociate the PMd from the frontal eye fields. In the present study, a pure eye-movement condition was not directly compared with the rotation conditions, and Talairach coordinates were used to identify individual regions. The Talairach coordinates re-

ported for the PMd in our article were also very similar (32 –11 48; –22 –11 48) to the coordinates reported by Jordan et al. (2002). The coordinates for the PMd given by Jordan et al. in MNI space were, on average, 28, –4, 56, which corresponds to the Talairach coordinates 23.8, –7, 48.6. However, as both regions are so close together that Talairach coordinates alone might not be specific enough to dissociate the PMd from the frontal eye fields, particular care should be taken in future research to dissociate these regions functionally.

It was further demonstrated, on the basis of an extended version of the Jordan model, that the inter-regional connectivity changes with the level of task difficulty. This implies that not all nodes of the network are functionally homogeneous but exhibit a differential functional involvement during task performance. Prior to the investigation of changes in effective connectivity across levels of task difficulty, a time-resolved fMRI analysis was carried out. This allowed us to identify changes in specific temporal characteristics of the HRF on the level of individual neuroanatomical nodes and to relate these alterations to the employed experimental design. It was found that the observed changes in connectivity on the network level were directly related to the results of the time-resolved fMRI analysis. No significant change in connectivity was observed within the visual components of the rotation network (i.e., OC, ITp, DE). The hemodynamic response in these regions is therefore either constant across conditions or changes with the level of task difficulty in a temporally coherent fashion. Time-resolved analysis has, however, shown that neither amplitude nor FWHM of the HRF in visual ROIs is correlated with RT measures. The analysis on the network level, as well as on the level of the individual network nodes, therefore converge in suggesting that the level of task difficulty does not affect the functional activation in visual regions. Instead, the results support previous statements suggesting that visual system activation during mental rotation reflects visual perception and can be dissociated from other network components whose response characteristics indicate an involvement in the mental spatial transformation itself (Ecker et al., 2006; Carpenter et al., 1999). No significant change in effective connection was also observed in the forward connection from the parietal ROI to the PMd, which is also in agreement with the time-resolved analysis. Although the HRF in visual regions did not change with RTs, there was a significant increase in FWHM in both the PMd and the parietal ROI. If the width of the HRF in both regions increases at about the same rate, no significant change in path coefficient should be observed. It therefore seems that the parietal ROI and the PMd are functionally coupled during task performance and the fMRI time series changes with the level of task difficulty in a similar fashion. In addition, the time course of activation in the PMd and PP can be dissociated from activation in the visual system as well as in the M1. This offers further support for the hypothesis that activation

in these regions is directly linked to the time course required for the computation of the spatial coordinates and that these regions are thus most likely to participate in the rotational process itself (Richter et al., 2000).

A significant change in connection strength from 0° to 100° rotation was observed in two connections exclusively: (1) the forward projection linking the DE with the PP, and (2) the path from the PMd to M1. As would be predicted on the basis of the time-resolved analysis, the path from DE to the PP increased significantly with the degree of angular rotation, whereas a significant decrease in path coefficient was seen in the projection from the PMd to M1. In the DE, the HRF was constantly elevated for 8.8 ± 1.4 sec in all rotation conditions. In the parietal ROI, however, the FWHM increased significantly with the degree of angular disparity. A significant increase in correlation coefficient between the DE and PP would be expected. An opposite trend was found in M1 and the PMd. In M1, the width of the HRF did not change significantly with RTs (average FWHM across rotation condition was equal to 4.74 sec), whereas there was a significant increase in FWHM in the PMd. Thus, as RTs increase with the degree of angular disparity, the functional coupling between the PMd and the M1 decreases. In the light of the time-resolved analysis, it would be incorrect to say that with increased task load, the PP receives enhanced input from the DE or that the input to M1 from the PMd is decreased. Instead of representing the influence one neuronal system exerts over another, the identified path coefficients in SEM seem to reflect the overall time course of the experiment.

These findings therefore demonstrate that the observed changes in connectivity on the network level are directly related to changes in temporal characteristics of the HRFs between the four different rotation conditions. The functional dissociation of ROIs on the basis of the network analysis may therefore change depending on the overall time course of the experiment and the way stimuli are presented (i.e., block design, event-related design). As SEM seems highly specific to the experimental design or condition, it should therefore only be interpreted in the context of that particular design/condition. Time-resolved fMRI might be used to guide the interpretation of the path coefficients across conditions and to predict changes in connectivity on the network level. This not only applies to SEM but also connectivity analysis in general.

This raises questions concerning the meaning and interpretation of path coefficients in general. Mathematically, path coefficients represent the response in a dependent variable to a unit change in an independent variable, as all other variables in the model are held constant (Bollen, 1989). In the context of fMRI, path coefficients have also been described as the average influence of one ROI onto another in a given time interval (McIntosh & Gonzalez-Lima, 1994). Furthermore, the strength and the sign of a path coefficient have been

used to describe the strength and nature of the investigated anatomical connection. Positive coefficients are believed to reflect neuronal excitation and negative coefficients may reflect neuronal inhibition (Jennings, McIntosh, & Kapur, 1998; Nyberg et al., 1996). This study has, however, shown that path coefficients mainly reflect changes in temporal characteristics of the HRF induced by the experimental design. Entirely different results would have been expected if a different experimental design had been used. In an alternate self-paced design, which has previously been used for many mental rotation studies, the stimulus duration ends with RT so that the stimulus duration and RT are equal (e.g., Seurinck, Vingerhoets, Vandemaele, Deblaere, & Achten, 2005). In this case, the width of the HRF would be the same in all conditions and no changes in connectivity would be expected across rotation conditions. For example, the path coefficient linking the DE with the PP would be expected to be constant across conditions if the time course required for visual perception was identical with the time course required for the mental spatial transformation (e.g., by presenting a fixation cross as soon as subjects indicate their decision). This prediction would still be valid even if the duration of the visual responses was not equal to the stimulus duration (i.e., transient responses in early visual areas). Changes in effective connections might thus only be detected when subprocesses are uncoupled.

Therefore, the optimal experimental design for connectivity analysis should thus aim to maximize region-specific alterations in the temporal characteristics of the HRF (i.e., signal width or onset) by subdividing the overall time course of the experiment into temporally distinct subprocesses (e.g., for cognition and perception). This way, a functional dissociation can be achieved on the network level. Temporal characteristics of the HRF can be altered maximally by using event-related paradigms. Block designs, on the other hand, primarily alter the amplitude of the HRF, whereas its time course is dominated by the fundamental frequency or duration of each block. However, as amplitude differences alone do not directly affect the correlation between two regions (see Figure 3), the use of block designs for connectivity analysis is questionable.

So far, the discussion has focussed on the absolute model fit of the Jordan model or, rather, the lack of it. The absolute model fit as a stand-alone index is, however, generally considered meaningless because it only indicates how well a postulated model reproduces the observed interregional correlation matrix. Any numerical definition of the “how well” is, however, arbitrary. Thus, the appropriateness of a particular model should, in principal, only be assessed by comparing it to alternative models. In the present study, we have further demonstrated that adding feedback connections to the Jordan model significantly improved the goodness. The original model was extended by anatomically plausible feedback connections from the PMd to the PP and from the PP to

the ITp and the DE. The connectivity in this model highlights the role of the parietal lobe as multimodal association areas, which receive input from multiple sensory regions (Lewis & Van Essen, 2000). Rather than being directly involved in the computation of the spatial coordinates, this model suggests a more integrative role of parietal regions mediating information processing between visual and frontal premotor regions. This seems to support a previous suggestion, namely, that parietal activation seems less directly linked to the computation of the spatial transformation as formerly hypothesized (Lamm, Windischberger, Moser, & Bauer, 2007; Ecker et al., 2006).

Finally, a few methodological limitations should be mentioned. Most importantly, an all-female subject group was examined in this investigation. There is growing evidence that there are gender-specific differences in performance on mental rotation tasks and in the associated patterns of cortical activation. Men generally display faster RTs and higher accuracy than women (Voyer, Voyer, & Bryden, 1995; Linn & Petersen, 1985). As mentioned in the Introduction, these behavioral differences are reflected in the involved cortical networks (Jordan et al., 2002). The female pathway exclusively was investigated in the present study and the results may be different in the male population. In addition, we examined ROIs in the left hemisphere only because activation in M1 was observed in the left hemisphere exclusively. Thus, the examination of the rotation network needs to be extended to reflect activation in both hemispheres and sexes.

In this investigation, SEM was carried out on the basis of the first eigentimeseries in ROIs. The first eigentimeseries can be compared to a weighted average of the regional time series in each individual subject. This was done in accordance to previous investigations (Gavrilescu et al., 2004; Honey et al., 2003). If SEM is carried out across an average response pattern, intersubject variability is discounted and data from different subjects are treated as if it came from the same subject. Therefore, alternative approaches might be used in the future to specifically account for intersubject variability in SEM. For instance, Mechelli, Penny, Price, Gitelman, and Friston (2002) suggested a multisubject network consisting of ROIs as well as different subjects. In this way, intersubject as well as condition-specific changes in effective connections can be detected (Mechelli et al., 2002). Another approach involves analyzing the data by performing subject-specific analyses (Goncalves, Hall, Johnsrude, & Haggard, 2001; Buchel & Friston, 1997).

To conclude, the neurocognitive model underlying mental rotation proposed by Jordan et al. (2002) should be considered a surface model only and a model with feedback projections provided a significantly improved fit to the observed interregional connectivity matrix. This finding challenges traditional cognitive models describing the complex cognitive process underlying mental rotation by a set of sequentially organized, functionally distinct process-

ing stages. The effective connectivity within this network, however, changes depending on the level of task difficulty. Although no significant change in connectivity was observed within the visual subcomponents of the network, the temporal characteristics of the HRF in the parietal lobe and in the PMd changed significantly with task demand. This suggests that the functional activation in these regions is associated with mental spatial transformation itself. Using time-resolved fMRI, we have further shown that the change in path coefficients is directly linked to the employed experimental design. The results of SEM in fMRI should therefore only be interpreted in the light of a specific experimental design and should not be considered as general indicators of an effective connection between nodes of a cognitive network.

Acknowledgments

We thank the Neuroimaging Research Group, Department of Neurology, Institute of Psychiatry, London for their support. We would also like to thank all participants who volunteered for this study and Chris Andrew for programming the paradigm.

Reprint requests should be sent to Christine Ecker, Brain Image Analysis Unit, Centre for Neuroimaging Sciences (CNS), Institute of Psychiatry, KCL, P.O. Box 89, DeCrespigny Park, London, SE5 8AF, or via e-mail: c.ecker@iop.kcl.ac.uk.

REFERENCES

- Alivisatos, B., & Petrides, M. (1997). Functional activation of the human brain during mental rotation. *Neuropsychologia*, 35, 111–118.
- Barnes, J., Howard, R. J., Senior, C., Brammer, M., Bullmore, E. T., Simmons, A., et al. (2000). Cortical activity during rotational and linear transformations. *Neuropsychologia*, 38, 1148–1156.
- Beckmann, C. F., DeLuca, M., Devlin, J. T., & Smith, S. M. (2005). Investigations into resting-state connectivity using independent component analysis. *Philosophical Transactions of the Royal Society of London, Series B, Biological Sciences*, 360, 1001–1013.
- Bentler, P. M. (1980). Multivariate analysis with latent variables: Causal modelling. *Annual Review of Psychology*, 88, 419–456.
- Bentler, P. M., & Bonett, D. C. (1980). Significance tests and goodness of fit in the analysis of covariance structures. *Psychological Bulletin*, 88, 588–606.
- Bollen, K. A. (1989). *Structural equations with latent variables*. New York: Wiley.
- Brammer, M. J., Bullmore, E. T., Simmons, A., Williams, S. C., Grasby, P. M., Howard, R. J., et al. (1997). Generic brain activation mapping in functional magnetic resonance imaging: A nonparametric approach. *Magnetic Resonance Imaging*, 15, 763–770.
- Buchel, C., Coull, J. T., & Friston, K. J. (1999). The predictive value of changes in effective connectivity for human learning. *Science*, 283, 1538–1541.
- Buchel, C., & Friston, K. J. (1997). Modulation of connectivity in visual pathways by attention: Cortical interactions evaluated with structural equation modelling and fMRI. *Cerebral Cortex*, 7, 768–778.
- Bullmore, E., Horwitz, B., Honey, G., Brammer, M., Williams, S., & Sharma, T. (2000). How good is good enough in path analysis of fMRI data? *Neuroimage*, 11, 289–301.
- Bullmore, E., Long, C., Suckling, J., Fadili, J., Calvert, G., Zelaya, F., et al. (2001). Colored noise and computational inference in neurophysiological (fMRI) time series analysis: Resampling methods in time and wavelet domains. *Human Brain Mapping*, 12, 61–78.
- Bullmore, E. T., Suckling, J., Overmeyer, S., Rabe-Hesketh, S., Taylor, E., & Brammer, M. J. (1999). Global, voxel, and cluster tests, by theory and permutation, for a difference between two groups of structural MR images of the brain. *IEEE Transactions in Medical Imaging*, 18, 32–42.
- Carpenter, P. A., Just, M. A., Keller, T. A., Eddy, W., & Thulborn, K. (1999). Graded functional activation in the visuospatial system with the amount of task demand. *Journal of Cognitive Neuroscience*, 11, 9–24.
- Cohen, M. S., Kosslyn, S. M., Breiter, H. C., DiGirolamo, G. J., Thompson, W. L., Anderson, A. K., et al. (1996). Changes in cortical activity during mental rotation. A mapping study using functional MRI. *Brain*, 119, 89–100.
- Corballis, M. C. (1988). Distinguishing clockwise from counterclockwise: Does it require mental rotation? *Memory & Cognition*, 16, 567–578.
- Ecker, C., Brammer, M. J., David, A. S., & Williams, S. C. (2006). Time-resolved fMRI of mental rotation revisited—Dissociating visual perception from mental rotation in female subjects. *Neuroimage*, 32, 432–444.
- Farah, M. J. (1995). Current issues in the neuropsychology of image generation. *Neuropsychologia*, 33, 1455–1471.
- Fletcher, P., Buchel, C., Josephs, O., Friston, K., & Dolan, R. (1999). Learning-related neuronal responses in prefrontal cortex studied with functional neuroimaging. *Cerebral Cortex*, 9, 168–178.
- Formisano, E., Linden, D. E., Di Salle, F., Trojano, L., Esposito, F., Sack, A. T., et al. (2002). Tracking the mind's image in the brain: I. Time-resolved fMRI during visuospatial mental imagery. *Neuron*, 35, 185–194.
- Friston, K. J., & Buchel, C. (2000). Attentional modulation of effective connectivity from V2 to V5/MT in humans. *Proceedings of the National Academy of Sciences, U.S.A.*, 97, 7591–7596.
- Friston, K. J., Frith, C. D., Liddle, P. F., & Frackowiak, R. S. (1993). Functional connectivity: The principal-component analysis of large (PET) data sets. *Journal of Cerebral Blood Flow and Metabolism*, 13, 5–14.
- Ganis, G., Keenan, J. P., Kosslyn, S. M., & Pascual-Leone, A. (2000). Transcranial magnetic stimulation of primary motor cortex affects mental rotation. *Cerebral Cortex*, 10, 175–180.
- Gauthier, I., Hayward, W. G., & Tarr, M. J. (2002). BOLD activity during mental rotation and viewpoint-dependent object recognition. *Neuron*, 34, 161–171.
- Gavrilescu, M., Stuart, G. W., Waites, A., Jackson, G., Svalbe, I. D., & Egan, G. F. (2004). Changes in effective connectivity models in the presence of task-correlated motion: An fMRI study. *Human Brain Mapping*, 21, 49–63.
- Goebel, R., Linden, D. E., Lanfermann, H., Zanella, F. E., & Singer, W. (1998). Functional imaging of mirror and inverse reading reveals separate coactivated networks for oculomotion and spatial transformations. *NeuroReport*, 9, 713–719.
- Goncalves, M. S., Hall, D. A., Johnsrude, I. S., & Haggard, M. P. (2001). Can meaningful effective connectivities be obtained between auditory cortical regions? *Neuroimage*, 14, 1353–1360.
- Grady, C. L., Furey, M. L., Pietrini, P., Horwitz, B., & Rapoport, S. I. (2001). Altered brain functional connectivity and impaired short-term memory in Alzheimer's disease. *Brain*, 124, 739–756.
- Harris, I. M., Egan, G. F., Sonkkila, C., Tochon-Danguy, H. J., Paxinos, G., & Watson, J. D. (2000). Selective right parietal lobe activation during mental rotation: A parametric PET study. *Brain*, 123, 65–73.

- Heil, M., Rauch, M., & Hennighausen, E. (1998). Response preparation begins before mental rotation is finished: Evidence from event-related brain potentials. *Acta Psychologica (Amsterdam)*, 99, 217–232.
- Honey, G. D., Suckling, J., Zelaya, F., Long, C., Routledge, C., Jackson, S., et al. (2003). Dopaminergic drug effects on physiological connectivity in a human cortico-striato-thalamic system. *Brain*, 126, 1767–1781.
- Horwitz, B., Deiber, M. P., Ibanez, V., Sadato, N., & Hallett, M. (2000). Correlations between reaction time and cerebral blood flow during motor preparation. *Neuroimage*, 12, 434–441.
- Iwaki, S., Ueno, S., Imada, T., & Tonoike, M. (1999). Dynamic cortical activation in mental image processing revealed by biomagnetic measurement. *NeuroReport*, 10, 1793–1797.
- James, L. R., Mulaik, S. A., & Brett, J. M. (1982). *Causal analysis: Assumptions, models, and data*. Sage: Beverly Hills, CA.
- Jennings, J. M., McIntosh, A. R., & Kapur, S. (1998). Mapping neural interactivity onto regional activity: An analysis of semantic processing and response mode interactions. *Neuroimage*, 7, 244–254.
- Jordan, K., Wustenberg, T., Heinze, H. J., Peters, M., & Jancke, L. (2002). Women and men exhibit different cortical activation patterns during mental rotation tasks. *Neuropsychologia*, 40, 2397–2408.
- Kline, R. B. (1998). *Principles and practice of structural equation modeling*. New York: Guilford Press.
- Kosslyn, S. M., DiGirolamo, G. J., Thompson, W. L., & Alpert, N. M. (1998). Mental rotation of objects versus hands: Neural mechanisms revealed by positron emission tomography. *Psychophysiology*, 35, 151–161.
- Kosslyn, S. M., Ganis, G., & Thompson, W. L. (2001). Neural foundations of imagery. *Nature Reviews Neuroscience*, 2, 635–642.
- Kosslyn, S. M., Maljkovic, V., Hamilton, S. E., Horwitz, G., & Thompson, W. L. (1995). Two types of image generation: Evidence for left and right hemisphere processes. *Neuropsychologia*, 33, 1485–1510.
- Kwong, K. K., Belliveau, J. W., Chesler, D. A., Goldberg, I. E., Weisskoff, R. M., Poncelet, B. P., et al. (1992). Dynamic magnetic resonance imaging of human brain activity during primary sensory stimulation. *Proceedings of the National Academy of Sciences, U.S.A.*, 89, 5675–5679.
- Lamm, C., Windischberger, C., Moser, E., & Bauer, H. (2007). The functional role of dorso-lateral premotor cortex during mental rotation: An event-related fMRI study separating cognitive processing steps using a novel task paradigm. *Neuroimage*, 36, 1374–1386.
- Lewis, J. W., & Van Essen, D. C. (2000). Corticocortical connections of visual, sensorimotor, and multimodal processing areas in the parietal lobe of the macaque monkey. *Journal of Comparative Neurology*, 428, 112–137.
- Linn, M. C., & Petersen, A. C. (1985). Emergence and characterization of sex differences in spatial ability: A meta-analysis. *Child Development*, 56, 1479–1498.
- Mardia, K. V. (1974). Applications of some measures of multivariate skewness and kurtosis in testing normality and robustness studies. *Sankhya Series B*, 36, 115–128.
- Matelli, M., Luppino, G., & Rizzolatti, G. (1991). Architecture of superior and mesial area 6 and the adjacent cingulate cortex in the macaque monkey. *Journal of Comparative Neurology*, 311, 445–462.
- McIntosh, A. R., & Gonzalez-Lima, F. (1994). Network interactions among limbic cortices, basal forebrain, and cerebellum differentiate a tone conditioned as a Pavlovian excitator or inhibitor: Fluorodeoxyglucose mapping and covariance structural modeling. *Journal of Neurophysiology*, 72, 1717–1733.
- Mechelli, A., Penny, W. D., Price, C. J., Gitelman, D. R., & Friston, K. J. (2002). Effective connectivity and intersubject variability: Using a multisubject network to test differences and commonalities. *Neuroimage*, 17, 1459–1469.
- Mechelli, A., Price, C. J., Friston, K. J., & Ishai, A. (2004). Where bottom-up meets top-down: Neuronal interactions during perception and imagery. *Cerebral Cortex*, 14, 1256–1265.
- Nyberg, L., McIntosh, A. R., Cabeza, R., Nilsson, L. G., Houle, S., Habib, R., et al. (1996). Network analysis of positron emission tomography regional cerebral blood flow data: Ensemble inhibition during episodic memory retrieval. *Journal of Neuroscience*, 16, 3753–3759.
- Parsons, L. M., Fox, P. T., Downs, J. H., Glass, T., Hirsch, T. B., Martin, C. C., et al. (1995). Use of implicit motor imagery for visual shape discrimination as revealed by PET. *Nature*, 375, 54–58.
- Picard, N., & Strick, P. L. (2001). Imaging the premotor areas. *Current Opinion in Neurobiology*, 11, 663–672.
- Podzebenko, K., Egan, G. F., & Watson, J. D. (2002). Widespread dorsal stream activation during a parametric mental rotation task, revealed with functional magnetic resonance imaging. *Neuroimage*, 15, 547–558.
- Richter, W., Somorjai, R., Summers, R., Jarmasz, M., Menon, R. S., Gati, J. S., et al. (2000). Motor area activity during mental rotation studied by time-resolved single-trial fMRI. *Journal of Cognitive Neuroscience*, 12, 310–320.
- Richter, W., Ugurbil, K., Georgopoulos, A., & Kim, S. G. (1997). Time-resolved fMRI of mental rotation. *NeuroReport*, 8, 3697–3702.
- Ruthruff, E., & Miller, J. (1995). Can mental rotation begin before perception finishes? *Memory & Cognition*, 23, 408–424.
- Sakata, H., & Kusunoki, M. (1992). Organization of space perception: Neural representation of three-dimensional space in the posterior parietal cortex. *Current Opinion in Neurobiology*, 2, 170–174.
- Seurinck, R., Vingerhoets, G., Vandemaele, P., Deblaere, K., & Achten, E. (2005). Trial pacing in mental rotation. *Neuroimage*, 25, 1187–1196.
- Shendan, H. E., & Kutas, M. (2007). Neurophysiological evidence for the time course of activation of global shape, part, and local contour representation during visual object categorization and memory. *Journal of Cognitive Neuroscience*, 19, 734–749.
- Shendan, H. E., & Stern, C. E. (2007). Mental rotation and object categorization share a common network of prefrontal and dorsal and ventral regions of posterior cortex. *Neuroimage*, 35, 1264–1277.
- Shepard, R. N., & Cooper, L. A. (1982). Mental images and their transformations. *Science*, 171, 701–703.
- Shepard, R. N., & Metzler, J. (1971). Mental rotation of three-dimensional objects. *Science*, 171, 701–703.
- Steiger, J. H. (1990). Structural model evaluation and modification: An interval estimation approach. *Multivariate Behavioral Research*, 25, 173–180.
- Talairach, J., & Tournoux, P. (1988). *Co-planar stereotaxic atlas of a human brain*. Thieme: Stuttgart.
- Tian, L., Jiang, T., Wang, Y., Zang, Y., He, Y., Liang, M., et al. (2006). Altered resting-state functional connectivity patterns of anterior cingulate cortex in adolescents with attention deficit hyperactivity disorder. *Neuroscience Letters*, 400, 39–43.
- Vingerhoets, G., de Lange, F. P., Vandemaele, P., Deblaere, K., & Achten, E. (2002). Motor imagery in mental rotation: An fMRI study. *Neuroimage*, 17, 1623–1633.
- Voyer, D., Voyer, S., & Bryden, M. P. (1995). Magnitude of sex differences in spatial abilities: A meta-analysis and consideration of critical variables. *Psychological Bulletin*, 117, 250–270.

This article has been cited by:

1. Wei Hu, Yong Lu, Changling Ren, John X. Zhang. 2013. ERP evidence for the time course of mental rotation in the mirror reading of Chinese words. *Neuroscience Letters* **552**, 151-155. [[CrossRef](#)]
2. Jane McGrath, Katherine Johnson, Christine Ecker, Erik O'Hanlon, Michael Gill, Louise Gallagher, Hugh Garavan. 2012. Atypical Visuospatial Processing in Autism: Insights from Functional Connectivity Analysis. *Autism Research* **5**:10.1002/aur.v5.5, 314-330. [[CrossRef](#)]
3. Kerstin Paschke, Kirsten Jordan, Torsten Wüstenberg, Jürgen Baudewig, Jürgen Leo Müller. 2012. Mirrored or identical — Is the role of visual perception underestimated in the mental rotation process of 3D-objects?: A combined fMRI-eye tracking-study. *Neuropsychologia* **50**, 1844-1851. [[CrossRef](#)]
4. Christian Hoppe, Klaus Fliessbach, Sven Stausberg, Jelena Stojanovic, Peter Trautner, Christian E. Elger, Bernd Weber. 2011. A key role for experimental task performance: Effects of math talent, gender and performance on the neural correlates of mental rotation. *Brain and Cognition* . [[CrossRef](#)]
5. Robert H. Logie, Cyril R. Pernet, Antimo Buonocore, Sergio Della Sala. 2011. Low and high imagers activate networks differentially in mental rotation. *Neuropsychologia* **49**, 3071-3077. [[CrossRef](#)]
6. Jing Sui, Tülay Adalı, Godfrey Pearlson, Honghui Yang, Scott R. Sponheim, Tonya White, Vince D. Calhoun. 2010. A CCA+ICA based model for multi-task brain imaging data fusion and its application to schizophrenia. *NeuroImage* **51**, 123-134. [[CrossRef](#)]
7. Chérif P. Sahyoun, John W. Belliveau, Isabelle Soulières, Shira Schwartz, Maria Mody. 2010. Neuroimaging of the functional and structural networks underlying visuospatial vs. linguistic reasoning in high-functioning autism. *Neuropsychologia* **48**, 86-95. [[CrossRef](#)]
8. Isabell Wartenburger, Hauke R. Heekeren, Franziska Preusse, Jürg Kramer, Elke van der Meer. 2009. Cerebral correlates of analogical processing and their modulation by training. *NeuroImage* **48**, 291-302. [[CrossRef](#)]
9. Hong Zhang, Yu Sun, Jing Yan, Jingjie Wang, Yihong Qiu, Yisheng Zhu, Shanbao Tong. 2009. Cortical interactive network during mental rotation of Chinese character. *Neuroscience Letters* **461**, 185-189. [[CrossRef](#)]